J. Fluid Mech. (2017), *vol.* 814, *pp.* 5–23.
doi:10.1017/jfm.2017.25

Modelling steady shear flows of Newtonian liquids with non-Newtonian interfaces

Patrick T. Underhill[1], **Amir H. Hirsa**[2,†] **and Juan M. Lopez**[3]

[1]Department of Chemical and Biological Engineering, Rensselaer Polytechnic Institute, Troy, NY 12180-3590, USA

[2]Department of Mechanical, Aerospace and Nuclear Engineering, Rensselaer Polytechnic Institute, Troy, NY 12180-3590, USA

[3]School of Mathematical and Statistical Sciences, Arizona State University, Tempe, AZ 85287, USA

(Received 5 May 2016; revised 5 January 2017; accepted 5 January 2017; first published online 31 January 2017)

In countless biological and technological processes, the flow of Newtonian liquids with a non-Newtonian interface is a common occurrence, such as in monomolecular films in 'solid' phases atop of aqueous bulk fluid. There is a lack of models that can predict the flow under conditions different from those used to measure the rheological response of the interface. Here, we present a model which describes interfacial hydrodynamics, including two-way coupling to a bulk Newtonian fluid described by the Navier–Stokes equations, that allows for shear-thinning response of the interface. The model includes a constitutive equation for the interface under steady shear that takes the Newtonian functional form but where the surface shear viscosity is generalized to be a function of the local shear rate. In the limit of a highly viscous interface, the interfacial hydrodynamics is decoupled from the bulk flow and the model can be solved analytically. This provides not only insight into the flow but also a means to validate the numerical technique for solving the two-way coupled problem. The numerical results of the coupled problem shed new light on existing experimental results on steadily sheared monolayers of dipalmitoylphosphatidylcholine (DPPC), the primary constituent of lung surfactant and the bilayers of mammalian cell walls. For low packing density DPPC monolayers, a Newtonian shear-independent surface shear viscosity model can reproduce the interfacial flows, but at high packing density, the shear-thinning properties of the new model presented here are needed.

Key words: interfacial flows (free surface), non-Newtonian flows, rheology

1. Introduction

Predicting the flow of Newtonian interfaces is a mature science, whereas predictive modelling of non-Newtonian interfaces has yet to be demonstrated (Sagis 2011). In part, this stems from inherent difficulties in making experimental measurements of sheared viscous interfaces in a regime where the flows can be described using current models. One of the main hindrances has been the nonlinear two-way hydrodynamic

† Email address for correspondence: hirsaa@rpi.edu

coupling between the viscous interface and the fluid on which it lies (Reynaert *et al.* 2008; Dhar *et al.* 2010; Vandebril *et al.* 2010; Fuller & Vermant 2011; Langevin 2014*a*); both the interface and the bulk fluid are flowing and are viscously coupled. Many recent experiments designed to study the rheology of such systems have attempted to operate in regimes where the interfacial hydrodynamic coupling to the bulk flow is effectively negligible (Choi *et al.* 2011; Erni 2011; Kim *et al.* 2011). This occurs when $\mu^s/\mu L \to \infty$, where μ^s is the surface (excess) shear viscosity, μ is the bulk fluid's dynamic viscosity and L is the system's length scale. For a given physical system (such as an insoluble monolayer of a given surface concentration on water at a desired temperature), μ^s and μ are fixed. So, one is left with the length scale of the system, which is made as small as possible – leading to the now popular approach of using surface microrheology. This has led to insights into the microstructure and mesoscale responses of viscous interfaces, but has not provided consistent measurements of the macroscopic quantity μ^s. Estimates of μ^s from microrheology differ by orders of magnitude from estimates using conventional surface viscosity measurements (Ortega, Ritacco & Rubio 2010; Maestro *et al.* 2011; Fuller & Vermant 2012; Shlomovitz *et al.* 2013; Langevin 2014*b*; Gauchet, Durand & Langevin 2015), and so there is a lack of confidence in predictions from viscous interfacial hydrodynamic models using μ^s estimates derived from microrheology.

Another approach to measure μ^s entails fully accounting for the hydrodynamic coupling to the bulk flow and more directly measuring the macroscopic quantity μ^s. This has been done and gives consistent results between systems over various length scales and flow geometries when the surface concentration is low, and the result is generally that μ^s is small. When the surface concentration is not low, many interfaces of interest exhibit highly viscous behaviour that varies with the strength with which the interface is sheared. Here, we present a non-Newtonian interfacial model, which contains an interfacial Bingham fluid model as a special case, that is fully coupled to the bulk hydrodynamics and which shows that the coupled hydrodynamics agree very well with experimental measurements even in regimes where the surface concentration is very high (e.g. regimes that are anticipated to be found for *in vivo* respiratory systems). Non-Newtonian surface viscosity models have been previously proposed in order to help interpret experimental data (Kurnaz & Schwartz 1997; Ivanova, Ignes-Mullol & Schwartz 2001; Sagis 2010; Espinosa *et al.* 2011), but they do not include two-way coupling with the bulk hydrodynamics, as is done here.

A widely used method for the macroscopic measurement of surface shear viscosity is the deep-channel surface viscometer (Mannheimer & Schechter 1970; Edwards, Brenner & Wasan 1991). It shears the interface by the viscous coupling to the bulk flow that is driven by the rotating floor. However, deep-channel surface viscometers are of no utility for highly viscous interfaces because they are immobile due to nonlinearity in their constitutive relation, e.g. exhibit a yield stress or shear-thinning behaviour. In these situations, the vortex lines emanating from the rotating floor become parallel to the interface, as reported, for example, by Sadoughi, Lopez & Hirsa (2013) for monolayers of the lung surfactant dipalmitoylphosphatidylcholine (DPPC) when it is at large surface concentrations. Thus, in order to study the shear response of such highly viscous interfaces, the interfaces need to be driven directly, e.g. by moving a disc at the interface or a knife edge that is touching the interface. The use of a translating disc however has been shown to be ineffective in determining the shear rheological characteristics of such interfaces as it imparts a mixed-type flow with both shear and dilational components (Elfring, Leal & Squires 2016). In contrast, the knife-edge viscometer (and its variants) consisting of a sharp

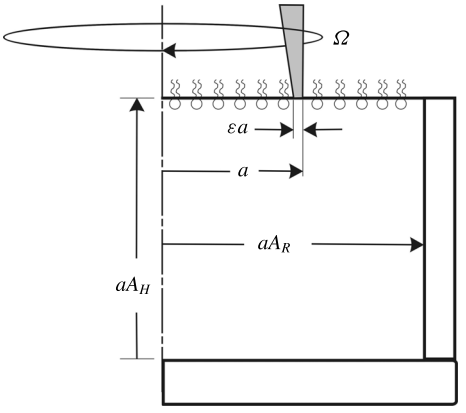

FIGURE 1. Schematic of the knife-edge viscometer, consisting of a stationary cylinder of radius aA_R filled to a height aA_H with a liquid of dynamic viscosity μ, on top of which is an interfacial monomolecular film. A circular knife edge of radius a and thickness ϵa just touches the interface and is steadily rotating with angular speed Ω.

circular knife edge just touching the interface of a bulk liquid (typically water) in a stationary cylindrical container, with the knife edge concentric with the cylinder and rotating steadily, does impart a pure shear flow to the interface (Jiang, Chen & Slattery 1983). The knife-edge viscometer geometry is used in this study; a schematic is shown in figure 1.

In § 2, we generalize the constitutive relation for the interfacial stress in order to model shear-thinning responses that are observed experimentally in many interfaces. Analytical and semi-analytical results from the model are obtained in the limiting case of the interfacial flow being decoupled from the bulk flow. These are presented in § 3. For full two-way coupling between the interfacial and bulk flows, numerical simulations are needed. The numerical technique is presented in § 4 and the simulation results are presented in § 5, where comparisons with the analytic results are made in appropriate regimes and the effects of the two-way coupling are elucidated. In § 6, a discussion of the main results is presented and we demonstrate the applicability of the computational model by showing good agreement with the experimental results obtained by Raghunandan, Lopez & Hirsa (2015) on one of the most widely studied interfaces, namely DPPC on water.

2. Interfacial constitutive equations

The coupling of the interface and the bulk occurs because of a stress balance. The general version of the stress balance is given in Slattery, Sagis & Oh (2007). Ignoring the stresses from the air, this balance relates the liquid stress to the interfacial stress. We consider flows in cylindrical geometries, described using (dimensional) polar coordinates $(r^\star, \theta, z^\star)$ and corresponding velocity vector $(u^\star, v^\star, w^\star)$, in regimes where the flows remain axisymmetric. For a flat interface, the normal stress balance simply gives that the velocity component normal to the interface is zero, $w^\star = 0$. The radial stress balance can be simplified by observing that for any insoluble monomolecular film on the liquid, if the monolayer is at a high enough concentration (packing) to exhibit surface shear viscosity, then it is sufficiently stiff to resist radial motion. Thus, the radial stress balance is simply $u^\star = 0$. This is because it only takes a minuscule

surface tension gradient to overcome radial flow at such an interface (Hirsa, Lopez & Miraghaie 2002). That leaves only $v^\star$ at the interface to be determined from the interfacial stress balance in the θ direction, coupling the interfacial hydrodynamics and the bulk flow. The azimuthal interfacial stress balance is arrived at by taking the general stress balance equation, simplified with the above considerations, and dotting it with the unit vector in the azimuthal direction, $\hat{\boldsymbol{\theta}}$

$$\hat{\boldsymbol{\theta}} \cdot [\boldsymbol{\nabla}_s \cdot \tilde{\boldsymbol{\tau}}^s] - \hat{\boldsymbol{\theta}} \cdot \boldsymbol{\nabla}_s \sigma = \hat{\boldsymbol{\theta}} \cdot \tilde{\boldsymbol{\tau}} \cdot \hat{\boldsymbol{z}}, \tag{2.1}$$

where σ is the surface tension, $\hat{\boldsymbol{z}}$ is the unit vector in normal to the interface, $\tilde{\boldsymbol{\tau}}$ is the viscous stress of the bulk fluid evaluated at the interface and $\tilde{\boldsymbol{\tau}}^s$ is the difference between the total interfacial stress and the stress coming from surface tension. In component form, this azimuthal interfacial stress balance is

$$\frac{1}{r^{\star 2}} \frac{\partial}{\partial r^\star} \left(r^{\star 2} \tilde{\tau}^s_{r\theta} \right) = \mu \frac{\partial v^\star}{\partial z^\star}, \tag{2.2}$$

where μ is the dynamic viscosity of the bulk fluid and $\tilde{\tau}^s_{r\theta}$ is the shear component of the interfacial shear stress tensor.

In order to solve the coupled problem, we must have a constitutive equation for the interface that relates the stress in (2.2) to the interfacial velocity field. In steady shear, many interfaces show shear-thinning behaviour where the viscosity material function decreases with increasing shear rate (Slattery *et al.* 2007). Also, previous work with DPPC monolayers suggests that at low enough surface concentrations, the interface is Newtonian, while at higher surface concentrations the interface is shear thinning with a possible yield stress behaviour (Sadoughi *et al.* 2013; Raghunandan *et al.* 2015). This is based on measurements of flow and stresses at the interface as well as visualizations of co-existing phase domains of the monolayer. We will use a model that has a finite viscosity at all shear rates, even if that viscosity is very large, and introduce a non-Newtonian constitutive equation for steady shear flow that takes the Newtonian functional form but where the surface shear viscosity is generalized to be a function of the shear rate. For shearing interfacial flows, where there is no dilation, the viscous constitutive relation becomes

$$\tilde{\boldsymbol{\tau}}^s = 2\mu^s_{eff} \boldsymbol{D}^s, \tag{2.3}$$

where μ^s_{eff} is an effective surface shear viscosity, which is a function of the magnitude of the local shear rate $\dot{\gamma}$, and $\boldsymbol{D}^s$ is the surface rate of deformation tensor. For a cylindrical geometry, the interfacial shear rate is given by

$$\dot{\gamma} = \frac{\partial v^\star}{\partial r^\star} - \frac{v^\star}{r^\star}. \tag{2.4}$$

Here, 'deformation' refers to relative motion in the plane of the interface that is not rigid body motion, as opposed to transverse undulations and motions perpendicular to the interface. The form of the effective surface viscosity we use is motivated by the Carreau–Yasuda model for bulk materials (Bird, Armstrong & Hassager 1987). The effective surface viscosity used is

$$\mu^s_{eff} = \mu^s \left(\frac{\tilde{\tau}/\mu^s + |\dot{\gamma}|}{\tilde{\tau}/\mu^s_0 + |\dot{\gamma}|} \right), \tag{2.5}$$

where μ_0^s is the surface shear viscosity at zero shear rate, μ^s is the surface shear viscosity at infinite shear rate, and $\tilde{\tau}$ is a material parameter with units of interfacial stress that alters how μ_{eff}^s depends on shear rate. This choice is a subset of the functions typically used in a Carreau–Yasuda model that has the Bingham model as a special case, and is simple enough to perform some analytical calculations. In the limit of $\mu_0^s \to \infty$, the model becomes the interfacial equivalent of the Bingham model in which $\tilde{\tau}$ is the interfacial yield stress. Furthermore, if $\mu_0^s = \mu^s$ or $\tilde{\tau} = 0$, then the response is Newtonian.

In the steady cylindrical system used here, time is non-dimensionalized by the angular velocity of the knife edge, Ω, space is non-dimensionalized by the outer radius of the knife edge, a, and stress is non-dimensionalized by $\mu^s\Omega$. The three material properties in the constitutive equation lead to three dimensionless parameters,

$$Bo = \frac{\mu^s}{\mu a}, \quad \xi = \frac{\mu^s}{\mu_0^s}, \quad \tau = \frac{\tilde{\tau}}{\mu^s \Omega}. \tag{2.6a–c}$$

The first parameter, Boussinesq number Bo, is the ratio of interfacial shear viscosity at infinite shear rate to the dynamic viscosity of the bulk liquid times the length scale. The second parameter ξ, is the ratio of the two surface shear viscosities. For a shear-thinning material like DPPC, the value of ξ is less than one. At high surface concentration, we expect ξ to be very small. If $\xi \to 0$, the viscosity at zero shear rate becomes infinite and the model becomes the Bingham model. Note also that $\xi = 1$ corresponds to the Newtonian case, independent of the value of τ, since then the two surface shear viscosities at zero and infinite shear rates are the same. The third parameter τ can be interpreted as a dimensionless yield stress when ξ is small, and compares the typical viscous stress calculated using μ^s when sheared at Ω to the yield stress.

The non-dimensional shear rate is

$$S = \frac{\dot{\gamma}}{\Omega} = \frac{\partial v}{\partial r} - \frac{v}{r}. \tag{2.7}$$

With these non-dimensional quantities, equation (2.5) can be written as an effective Boussinesq number

$$Bo_{eff} = Bo\left(\frac{\tau + |S|}{\xi\tau + |S|}\right), \tag{2.8}$$

and (2.2) becomes

$$\frac{1}{r^2}\frac{\partial}{\partial r}\left(r^2 \tau_{r\theta}^s\right) = \frac{1}{Bo}\frac{\partial v}{\partial z}, \tag{2.9}$$

where

$$\tau_{r\theta}^s = \left(\frac{\tau + |S|}{\xi\tau + |S|}\right) S. \tag{2.10}$$

Substituting (2.10) into (2.9) gives the non-dimensional azimuthal stress balance at the interface. One form of this stress balance is

$$\frac{1}{r^2}\frac{\partial}{\partial r}\left(Bo_{eff}\, r^2 S\right) = \frac{\partial v}{\partial z}, \tag{2.11}$$

in which Bo_{eff} is inside the derivative because the effective shear viscosity depends on shear rate, which in turn depends on r. Upon substituting (2.8) for Bo_{eff} and (2.7) for S into (2.11), the azimuthal interfacial stress balance becomes

$$\left[1 + \frac{\xi\tau^2(1-\xi)}{(\xi\tau + |S|)^2}\right]\frac{\partial^2 v}{\partial r^2} + \left[1 + \frac{\tau(\xi\tau + 2|S|)(1-\xi)}{(\xi\tau + |S|)^2}\right]\left(\frac{1}{r}\frac{\partial v}{\partial r} - \frac{v}{r^2}\right) = \frac{1}{Bo}\frac{\partial v}{\partial z}. \tag{2.12}$$

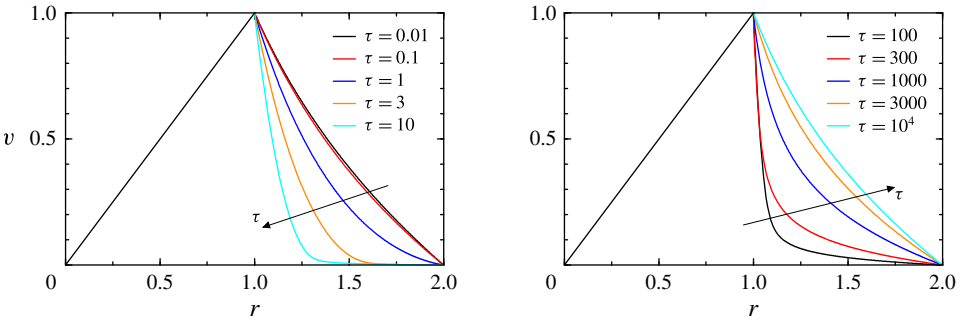

FIGURE 2. (Colour online) Profiles of azimuthal velocity v at the interface, determined in the limit $Bo \to \infty$ with $\xi = 10^{-3}$, $A_R = 2$, and τ as indicated; the results are independent of Re and ϵ.

3. Decoupled interfacial flow in the limit $Bo \to \infty$

In the limit $Bo \to \infty$, the interfacial hydrodynamics is completely decoupled from the bulk flow and can be solved independently. However, the bulk flow is still dependent on the interfacial flow, as will be shown later. In this limit, (2.9) reduces to

$$\frac{1}{r^2}\frac{\partial}{\partial r}(r^2\tau^s_{r\theta}) = 0, \tag{3.1}$$

which implies that $\tau^s_{r\theta} = -C/r^2$, where C is a constant of integration, determined by boundary conditions. For the region inside of the knife edge, $r \in [0, 1-\epsilon]$, where ϵ is the ratio of the knife-edge thickness to its outer radius, since $\tau^s_{r\theta}$ must be finite at $r = 0$, we must have $C = 0$ and so $\tau^s_{r\theta} = 0$. From (2.10), $\tau^s_{r\theta} = S(\tau + |S|)/(\xi\tau + |S|) = 0$. Since τ and ξ are strictly non-negative for the interfaces examined here, this implies $S = \partial v/\partial r - v/r = 0$, giving $v \propto r$, and with the boundary condition $v|_{r=1-\epsilon} = 1 - \epsilon$, gives $v = r$. In other words, the interfacial region inside the knife edge is in solid-body rotation with the knife edge.

The fluid in contact with the knife edge, $r \in [1-\epsilon, 1]$, is moving with it, and therefore $v = r$. Hence, in the limit $Bo \to \infty$, the thickness of the knife edge is irrelevant: $v = r$ for $r \in [0, 1]$ for any $\epsilon \in [0, 1]$, and the viscous interface on the inside of the knife edge acts identical to a rotating no-slip disc.

For the interface between the knife edge and the stationary cylinder, $r \in [1, A_R]$, where A_R is the ratio of the cylinder radius to the knife-edge radius, we have

$$\tau^s_{r\theta} = -C/r^2 = \left(\frac{\tau + |S|}{\xi\tau + |S|}\right) S. \tag{3.2}$$

For $r \in [1, A_R]$, the motion of the knife edge relative to the outer cylinder will make $S \leqslant 0$ so that $S = -|S|$, then

$$\frac{C}{r^2}(\xi\tau + |S|) = (\tau + |S|)|S|, \tag{3.3}$$

which can be solved for $|S|$. The resultant shear rate is then integrated to obtain the velocity, and the integration constants are determined by the boundary conditions. Figure 2 shows profiles of the azimuthal velocity at the interface in the limit $Bo \to \infty$,

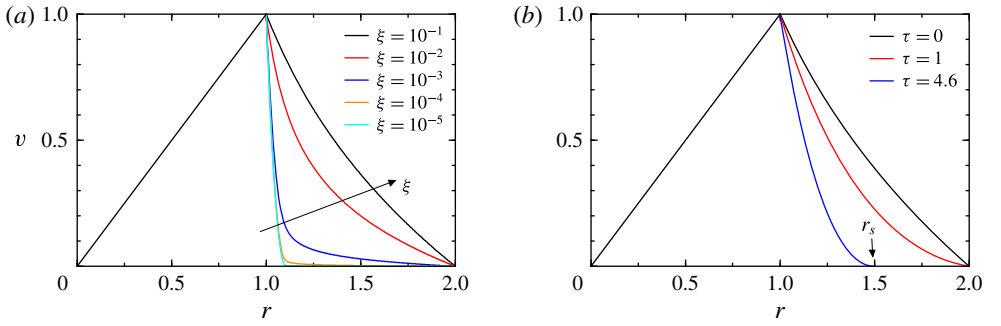

FIGURE 3. (Colour online) Profiles of azimuthal velocity v at the interface, determined in the limit $Bo \to \infty$ with $A_R = 2$, and (*a*) $\tau = 100$ and ξ as indicated, and (*b*) $\xi = 0$ (Bingham model) and τ as indicated. The results are independent of Re and ϵ.

determined from integrating the shear rate from (3.3) with $A_R = 2$, $\xi = 10^{-3}$ and τ covering six orders of magnitude. This radius ratio A_R matches that of the experiments in Raghunandan *et al.* (2015). For illustrative purposes, figure 3(*a*) shows how the interfacial azimuthal velocity profile varies with ξ for $\tau = 100$, for which $\xi \lesssim 10^{-3}$ is close to the Bingham limit. The analytic formulas for the profiles are detailed in appendix A. A better physical understanding for the dependence on τ can be gained by examining the approximate behaviour for small and large τ, which is done below. Figure 3(*b*) illustrates the behaviour of the Bingham model ($\xi = 0$), described later in (3.5).

Based on (2.8), the value of τ sets the shear rate above which the interface is approximately Newtonian. The value of $\xi\tau$ sets the shear rate below which the interface is also Newtonian but with a different viscosity. For $\tau \lesssim 10$, the velocity profiles in figure 2 are in close agreement with those for an interfacial Bingham model ($\xi = 0$). For small $\tau \lesssim 0.1$, the Newtonian velocity profile is essentially obtained, since τ is so small that the shear rate throughout the interface is always larger than τ.

Increasing τ changes the profile due to shear thinning; some parts of the interface are subjected to a shear rate that is less than τ and therefore exhibit a larger viscosity. The region near the knife edge, $r = 1$, has a higher shear rate and therefore exhibits a smaller viscosity compared to the region near the stationary cylinder wall at $r = 2$. In the range $1 < \tau < 10$, the shear rate near the outer cylinder approaches zero, and hence a portion of the interface near the cylinder is nearly stationary. For $\xi = 0$, the velocity profile continues to steepen with increasing τ. However, for $\xi \neq 0$ the velocity profile changes shape with increasing τ. Once $\xi\tau$ becomes larger than the local shear rate at the interface, the interface becomes Newtonian again. For $\xi = 10^{-3}$, this occurs when $\tau \sim 10^4$.

Analytic results that are valid for both small and large τ can be obtained. In the limit $\xi \to 0$ (or $\xi\tau \ll |S|$), (3.3) reduces to

$$C/r^2 = \tau + |S|. \tag{3.4}$$

This is valid in the region $r \in [1, \sqrt{C/\tau}]$, where the interface has 'yielded'. The value of C is determined by the boundary conditions. For small enough τ, the whole interface has yielded. We define a variable r_s that is the radius where the interface becomes stationary, and is the smaller of $\sqrt{C/\tau}$ and A_R. If the whole interface has yielded, then $r_s = A_R$. However, if only part has yielded then $r_s < A_R$ and the position r_s is determined as part of the solution.

In the yielded region, $S = \partial v/\partial r - v/r = \tau - C/r^2$, which can be solved to give $v = \tau r \ln r + C/(2r) + Br$. The boundary conditions are $v|_{r=1} = 1$ and $v|_{r=r_s} = 0$, where r_s is the smaller of $\sqrt{C/\tau}$ and A_R. These boundary conditions give $B = 1 - C/2$ and $C = 2r_s^2(1 + \tau \ln r_s)/(r_s^2 - 1)$. The azimuthal velocity profile in the region $r \in [1, r_s]$ is then

$$v = \frac{r_s^2}{(r_s^2 - 1)r} - \frac{r}{r_s^2 - 1} + \tau \left[r \ln r + \left(\frac{1}{r} - r \right) \frac{r_s^2}{r_s^2 - 1} \ln r_s \right]. \tag{3.5}$$

The whole interface yields when $r_s = \sqrt{C/\tau} = A_R$, and this happens when τ has the critical value given by

$$\tau_c = \left(\tfrac{1}{2}(A_R^2 - 1) - \ln A_R \right)^{-1}. \tag{3.6}$$

For $\tau < \tau_c$, the whole interface is moving and $r_s = A_R$. For $\tau > \tau_c$, only part of the interface moves so that $r_s = \sqrt{C/\tau}$, where r_s is the solution to

$$\tau = \left(\tfrac{1}{2}(r_s^2 - 1) - \ln r_s \right)^{-1}. \tag{3.7}$$

In the yielded region, the shear rate is given by $S = \tau - C/r^2 = \tau + 2(r_s/r)^2(1 + \tau \ln r_s)/(r_s^2 - 1)$.

Predictions based on these equations are shown in figure 3(*b*). For $\tau = 0$ and $\tau = 1$, the whole interface yields, and the profile is given by (3.5) with $r_s = A_R$. Figure 3(*b*) illustrates that for $\tau = 4.6$, which is greater than τ_c, the interface near the outer cylinder is not moving. The profile is still given by equation (3.5), except that the value of r_s depends on τ and is determined from (3.7). As τ is increased, r_s approaches the knife edge at $r = 1$.

For small non-zero ξ, the interface does not have a yield stress but instead has a very large viscosity at small shear rates and stresses. Once τ increases enough such that $\xi\tau$ is comparable to the shear rate, then $|S|$ is likely smaller than τ (since we are examining the cases of small ξ). In the limit of $|S| \ll \tau$, (3.3) reduces to

$$\frac{C}{r^2}(\xi\tau + |S|) = \tau |S|, \tag{3.8}$$

which can be solved analytically for the shear rate. As done previously, the velocity profile can be obtained from the shear rate. The constant C, determined by the boundary conditions, is

$$C = \tau A_R^2[\exp(2/(\xi\tau)) - 1]/[A_R^2 \exp(2/(\xi\tau)) - 1]. \tag{3.9}$$

The velocity profile in terms of this constant is

$$v = r + \xi\tau r \left[\ln r - \frac{1}{2} \ln \left(\frac{r^2 - C/\tau}{1 - C/\tau} \right) \right]. \tag{3.10}$$

This profile is only accurate when the shear rate is small compared to τ. From this interfacial velocity profile, the shear rate is found and used to determine when the shear rate is small compared to τ. This sets the range of validity for this approximation, given by

$$\frac{1}{\tau} \lesssim \frac{\xi}{2} \ln \left[\frac{(1 + \xi)A_R^2 - 1}{\xi A_R^2} \right]. \tag{3.11}$$

For the cases shown in figure 2, with $\xi = 10^{-3}$ and $A_R = 2$, this condition is $\tau \gtrsim 300$. Therefore, the analytic expression (3.10) illustrates how the profile approaches the Newtonian profile as $\tau \to \infty$.

4. Coupling the non-Newtonian interface with the bulk flow: numerical technique

The fully coupled nonlinear model we present here is essentially the same as that in Lopez & Hirsa (2015) and Raghunandan *et al.* (2015), which had Bo independent of the shear rate (a Newtonian surface model), but here we replace Bo with Bo_{eff}, (2.8), which depends on the local shear rate, $S(r)$. The flow in the bulk is governed by the Navier–Stokes equations. For parameter regimes of interest, the flow remains axisymmetric and it is convenient to use the streamfunction–vorticity formulation, where the velocity and vorticity are related to the streamfunction ψ by

$$\boldsymbol{u} = (u, v, w) = \left(-\frac{1}{r}\frac{\partial \psi}{\partial z},\ v,\ \frac{1}{r}\frac{\partial \psi}{\partial r} \right), \tag{4.1}$$

$$\boldsymbol{\nabla} \times \boldsymbol{u} = \left(-\frac{1}{r}\frac{\partial rv}{\partial z},\ \eta,\ \frac{1}{r}\frac{\partial rv}{\partial r} \right), \tag{4.2}$$

where

$$\eta = -\frac{1}{r}\frac{\partial^2 \psi}{\partial z^2} - \frac{1}{r}\frac{\partial^2 \psi}{\partial r^2} + \frac{1}{r^2}\frac{\partial \psi}{\partial r}. \tag{4.3}$$

In this formulation, the non-dimensional Navier–Stokes equations are

$$\frac{\partial v}{\partial t} - \frac{1}{r}\frac{\partial \psi}{\partial z}\frac{\partial v}{\partial r} + \frac{1}{r}\frac{\partial \psi}{\partial r}\frac{\partial v}{\partial z} - \frac{v}{r^2}\frac{\partial \psi}{\partial z} = \frac{1}{Re}\left(\frac{\partial^2 v}{\partial z^2} + \frac{\partial^2 v}{\partial r^2} + \frac{1}{r}\frac{\partial v}{\partial r} - \frac{v}{r^2} \right), \tag{4.4}$$

$$\frac{\partial \eta}{\partial t} - \frac{1}{r}\frac{\partial \psi}{\partial z}\frac{\partial \eta}{\partial r} + \frac{1}{r}\frac{\partial \psi}{\partial r}\frac{\partial \eta}{\partial z} + \frac{\eta}{r^2}\frac{\partial \psi}{\partial z} - \frac{2v}{r}\frac{\partial v}{\partial z} = \frac{1}{Re}\left(\frac{\partial^2 \eta}{\partial z^2} + \frac{\partial^2 \eta}{\partial r^2} + \frac{1}{r}\frac{\partial \eta}{\partial r} - \frac{\eta}{r^2} \right), \tag{4.5}$$

where

$$Re = \Omega a^2/\nu \tag{4.6}$$

is the Reynolds number. One additional geometric parameter enters the coupled problem, the cylinder height to knife-edge radius ratio A_H (see the schematic in figure 1).

The boundary conditions in the bulk are no slip:

$$\text{Sidewall, } r = A_R : v = \psi = 0, \quad \eta = -\frac{1}{A_R}\frac{\partial^2 \psi}{\partial r^2}, \tag{4.7}$$

$$\text{Bottom, } z = 0 : v = \psi = 0, \quad \eta = -\frac{1}{r}\frac{\partial^2 \psi}{\partial z^2}, \tag{4.8}$$

$$\text{Axis, } r = 0 : v = \psi = 0, \quad \frac{\partial \eta}{\partial r} = 0, \tag{4.9}$$

where the axis boundary condition is the symmetry condition for axisymmetric flow. As discussed in § 2, $u = w = 0$ at the interface $z = A_H$, and these imply that $\psi = 0$ and $\eta = -1/r\partial^2\psi/\partial z^2$ at the interface. The azimuthal velocity v at the interface is given by the solution to (2.12).

The numerical technique used is essentially the same as that used to solve the knife-edge viscometer flow in Lopez & Hirsa (2015). The only difference is that here, the interface is non-Newtonian, with the azimuthal stress balance described by (2.12). Taking $\tau = 0$ reduces (2.12) to the Newtonian azimuthal stress balance used in Lopez & Hirsa (2015). The equation is essentially a linear second-order ordinary differential

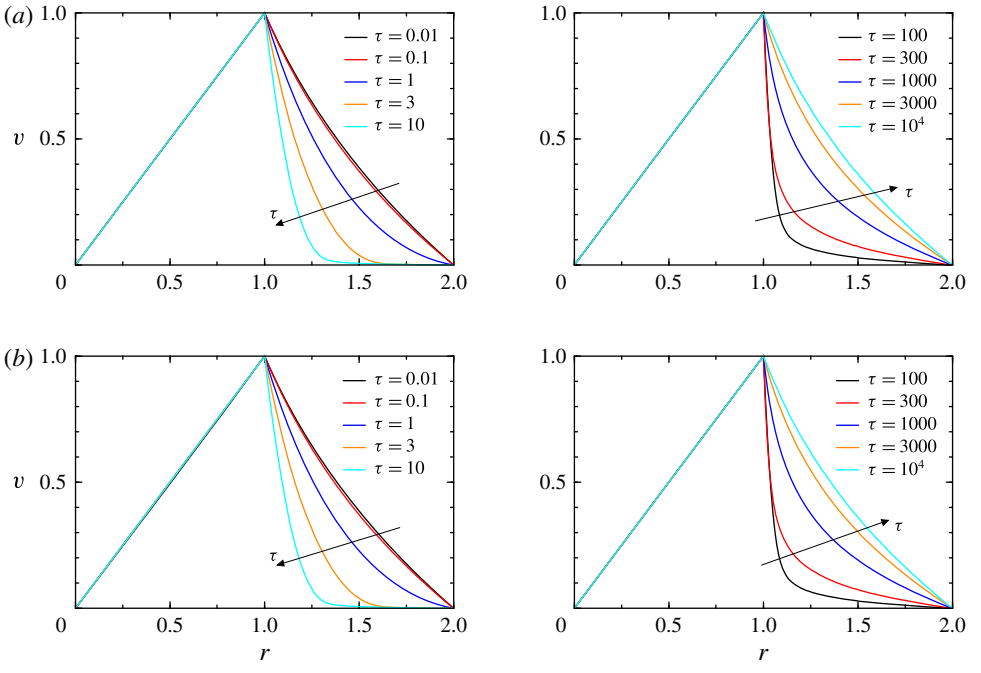

FIGURE 4. (Colour online) Radial profiles of v at the interface with $Bo = 100$, $\epsilon = 0.02$, $A_R = A_H = 2$, $\xi = 10^{-3}$ and τ as indicated, for (*a*) $Re = 1$ and (*b*) $Re = 10^3$.

equation for v at the interface, except that $\partial v/\partial z$ appears on the right-hand side of the equation. In Lopez & Hirsa (2015), $\partial v/\partial z$ is treated as 'known' by using its value from the previous time step. In fact, since the time integration is a two-stage Huen's method, the stress balance equation at the first stage is solved using $\partial v/\partial z$ from the previous time, then for the second (corrector) stage, $\partial v/\partial z$ is evaluated using the first (predictor) stage estimate of v. In the present problem, we use the same strategy for $|S| = |\partial v/\partial z - v/r|$ in the 'coefficients' on the left-hand side of (2.12). The equations are discretized using second-order centred finite differences, and all the results presented were computed using 201 grid points in both r and z, with $A_R = A_H = 2$. The time step depended on Re; $\delta t = 2 \times 10^{-5}$ for $Re = 1$ and $\delta t = 2 \times 10^{-3}$ for $Re = 10^3$. Grid resolution studies on the Newtonian interface problem were conducted in Lopez & Hirsa (2015) and the non-Newtonian problem does not change the grid requirements. Starting from rest, steady state is reached in approximately two viscous times, corresponding to $2Re$ time units, the factor 2 coming from A_R and A_H. In dimensional terms, one viscous time is a^2/ν seconds.

5. Simulations of the coupled flow

Simulations at $Bo = 100$ are presented in figure 4 for a wide range of τ and two values of Re. The velocity profiles are indistinguishable from the 'analytic' results, consistent with earlier findings that for knife-edge flow $Bo = 100$ is essentially at the limit $Bo \to \infty$ (Lopez & Hirsa 2015). Furthermore, this excellent agreement between the simulations at large Bo (figure 4) and the analytic interface solutions at $Bo = \infty$ (figure 2) provides validation that the numerics are solving the model correctly (verification that the model is relevant to physical systems requires comparison with

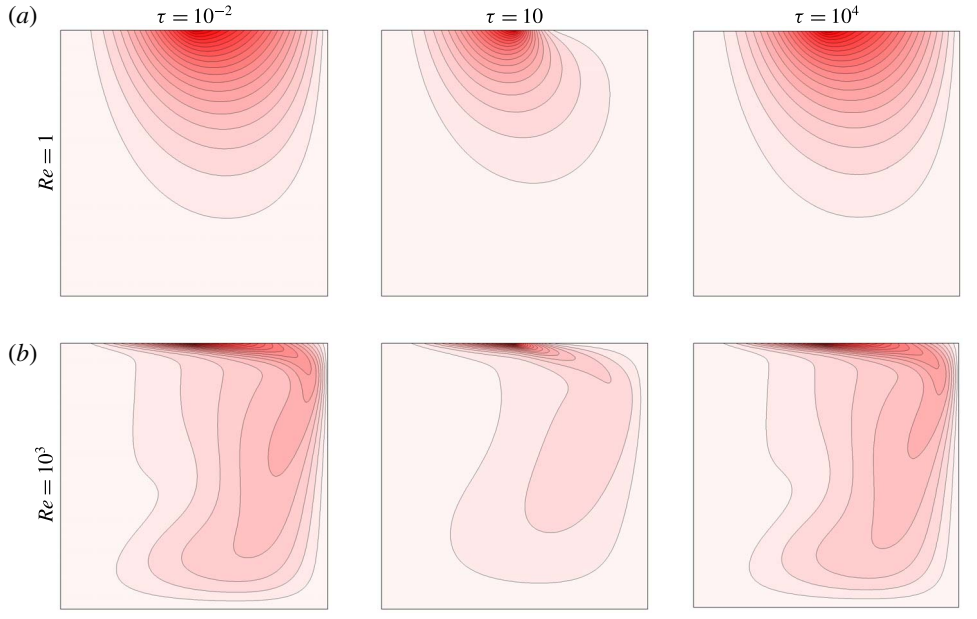

FIGURE 5. (Colour online) Vortex lines (isocontours of rv) at $Bo = 100$, $\xi = 10^{-3}$, $\epsilon = 0.02$, $A_R = A_H = 2$ for Re and τ as indicated, in a meridional plane $(r, z) \in [0, A_r] \times [0, A_z]$; there are 20 isocontours in the range [0, 1].

experimental data; this is addressed in § 6). In this large surface shear viscosity limit, the interface is not influenced by the flow in the bulk. This is illustrated by the fact that the interfacial velocity profile is independent of Re. However, the bulk flow is strongly dependent on Re, even though it is driven by the same boundary condition, namely the azimuthal interfacial velocity shown in figure 4. Figure 5 shows the vortex lines for $Re = 1$, which is in the Stokes flow regime with a viscous-dominated bulk flow, and $Re = 10^3$ with a nonlinear advection-dominated bulk flow where the vortex lines near the interface are swept radially outward by the induced meridional flow caused by the bending of the vortex lines (Lopez & Hirsa 2015). As noted in § 3, the interfacial flows in the small and large τ limits converge to the same flow, and figure 5 shows that the bulk flows at small and large τ are virtually the same for a given Re, but of course they are very different for different Re.

Figure 6 shows the interfacial velocity profiles for the same parameters as in figure 4, but for $Bo = 1$ instead of $Bo = 100$. The figure shows that for $\tau \gtrsim 100$, the results are indistinguishable between those for $Bo = 100$ and $Bo = 1$; for the Re values considered and large τ, the effective Bo_{eff} is essentially in the infinite limit and the interfacial flow is decoupled from the bulk flow. For $\tau = 10$ however, the interfacial flow for $Re = 10^3$ begins to deviate from that at $Re = 1$, which itself is the same as the analytic flow at $Bo = \infty$ (compare figures 2 and 6; the $Re = 10^3$ case at $Bo = 1$ has smaller Bo_{eff} and the coupling with the bulk flow leads to an altered interfacial flow). For $Re = 1$, the coupling with the bulk flow begins to be important for $\tau \lesssim 3$, showing departures from the solid-body rotation of the decoupled interface on the inner region, $r \in [0, 1 - \epsilon]$. These departures are more significant for the $Re = 10^3$ cases.

At the small $Bo = 10^{-2}$, figure 7 shows that for small to medium $\tau \lesssim 10$ the flow essentially corresponds to that of an inviscid interface for both $Re = 1$ and $Re = 10^3$.

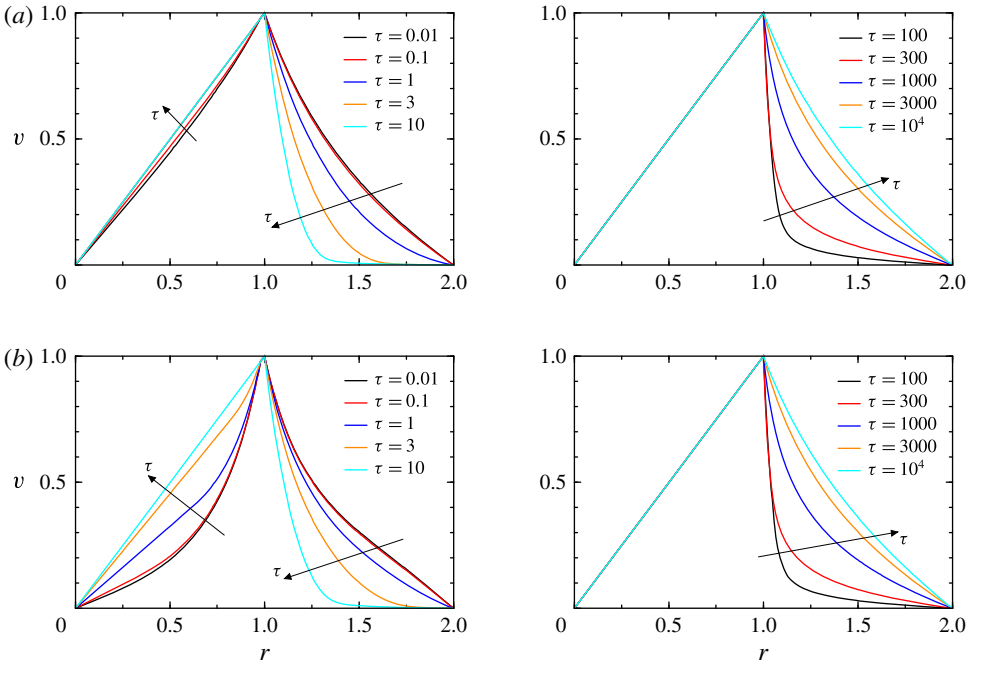

FIGURE 6. (Colour online) Radial profiles of v at the interface with $Bo = 1$, $\epsilon = 0.02$, $A_R = A_H = 2$, $\xi = 10^{-3}$ and τ as indicated, for (*a*) $Re = 1$ and (*b*) $Re = 10^3$.

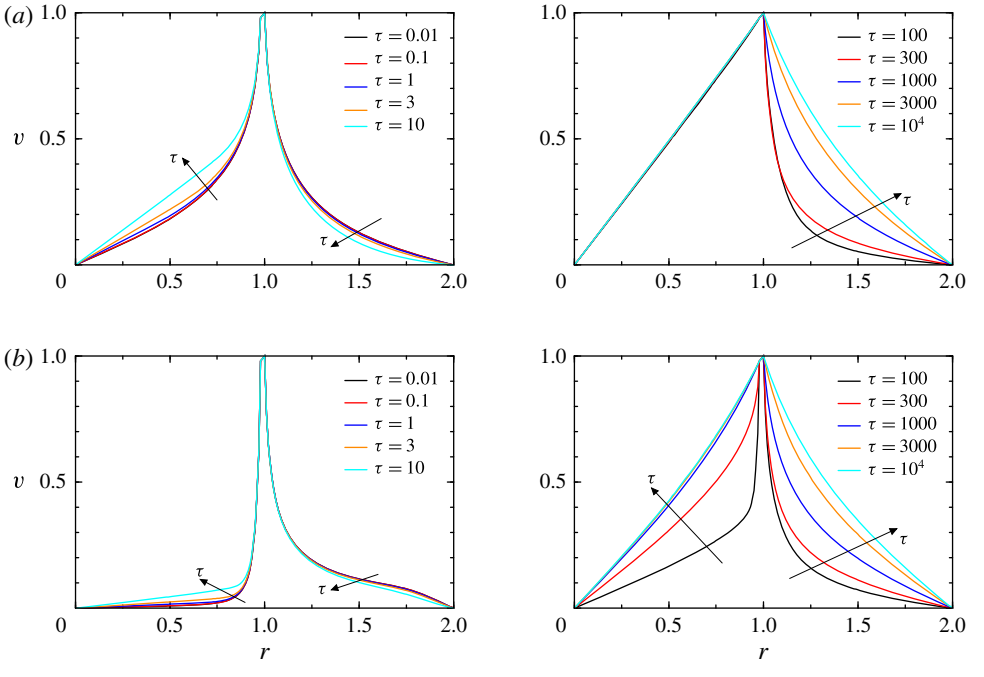

FIGURE 7. (Colour online) Radial profiles of v at the interface with $Bo = 10^{-2}$, $\epsilon = 0.02$, $A_R = A_H = 2$, $\xi = 10^{-3}$ and τ as indicated, for (*a*) $Re = 1$ and (*b*) $Re = 10^3$.

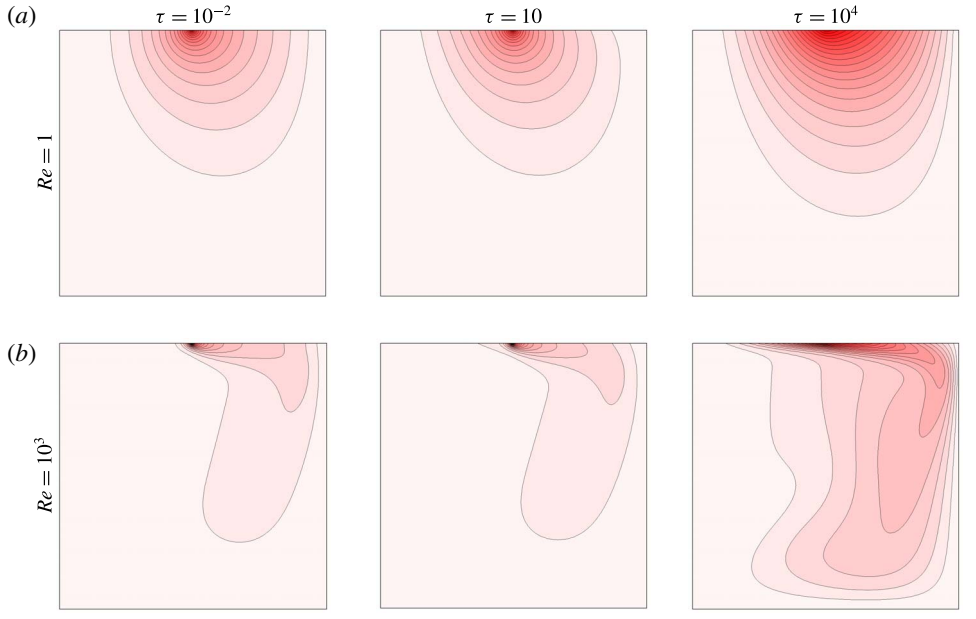

FIGURE 8. (Colour online) Vortex lines (isocontours of rv) at $Bo = 10^{-2}$, $\xi = 10^{-3}$, $\epsilon = 0.02$, $A_R = A_H = 2$ for Re and τ as indicated, in a meridional plane $(r, z) \in [0, A_r] \times [0, A_z]$; there are 20 isocontours in the range [0, 1].

However, the interfacial flows at the two Re are very different, and this is a result of the interface being driven by a viscous-dominated bulk flow in the low Re case and a very nonlinear bulk flow in the high Re case. These bulks flows are shown in figure 8. For $Re = 1$, figure 7(*a*) shows a dramatic transition in the interfacial flow on the inside of the knife edge as τ is increased from 10 to 100; the interfacial velocity snaps into a solid-body rotation profile. This indicates that due to the very low interfacial shear on the inside region at this low Re, Bo_{eff} becomes non-negligible. For the $Re = 10^3$ case, this transition is much more gradual as larger τ values are required to make the interface effectively viscous.

6. Discussion and conclusions

The new model for steadily sheared flow of a non-Newtonian interface of a Newtonian liquid presented here shows the impact of a shear-thinning interface in the knife-edge geometry. Salient features of the shear-thinning response that were captured include the solid-body rotation of the interface in the region inside the knife edge, as well as flow that is significantly retarded near the cylinder wall. In the limit of large Boussinesq number (relatively large surface shear viscosity), where the interfacial flow becomes independent of the bulk flow, the numerical model was validated against analytical solutions. In order to verify that the model predictions are relevant for physical systems, comparisons with experiments need to be made.

Measurements of the velocity field in the bulk and near the surface were recently reported (Raghunandan *et al.* 2015) for DPPC, the primary constituent of lung surfactant and bilayers making up our cell walls. Monolayers of DPPC were studied in a knife-edge flow apparatus with radius ratio $A_R = 2$, depth ratio $A_H = 2$, and

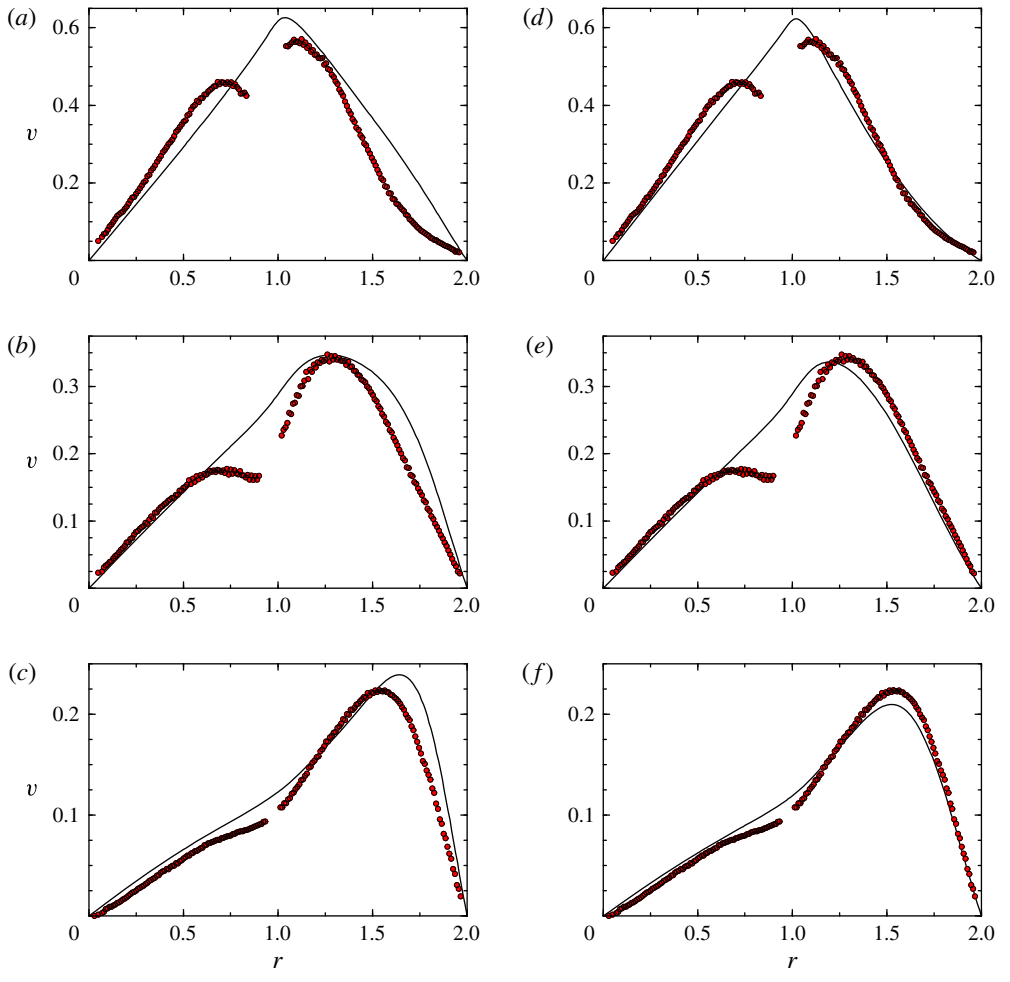

FIGURE 9. (Colour online) Comparisons between azimuthal velocity profiles determined experimentally in a knife-edge viscometer with a monolayer of DPPC at surface pressure 40 dyn cm^{-1} measured by PIV (symbols) from Raghunandan *et al.* (2015) with numerical profiles (lines) with (*a,b,c*) $Bo = 10$ and $\tau = 0$ (viscous Newtonian interface) and (*d,e,f*) $Bo = 3$, $\tau = 1$ and $\xi = 10^{-3}$, all with $Re = 300$, at depths (*a,d*) 4 %, (*b,e*) 10 % and (*c,f*) 20 % of the knife-edge radius below the interface.

knife-edge thickness ratio $\epsilon = 0.02$. The measurements were conducted using particle image velocimetry (PIV), which requires seeding particles. The combination of seeding particles and laser sheet illumination using a source that is sufficiently powerful to illuminate a wide swath of the 5 cm diameter of the cylinder used, resulted in a thermal loading on the system that locally induced thermal convection. In that study, it was found that flow at $Re \sim 30$ was significantly affected by this laser heating. The study also reported data at $Re = 100$ and 300. Here, we only consider the $Re = 300$ data which have the smallest effects of the laser-induced convection.

Figure 9 shows measurements (symbols) reported by Raghunandan *et al.* (2015) which were taken at depths of 4 %, 10 % and 20 % of the knife-edge radius. It is important to note that velocity measurements were not reliable near the knife edge,

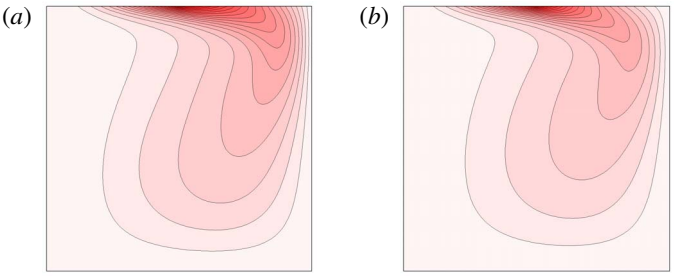

FIGURE 10. (Colour online) Vortex lines (isocontours of rv) at $Re = 300$ with (*a*) $Bo = 10$ and $\tau = 0$ (viscous Newtonian interface) and (*b*) $Bo = 3$, $\tau = 1$ and $\xi = 10^{-3}$, in a meridional plane $(r, z) \in [0, A_r] \times [0, A_z]$; there are 20 isocontours in the range [0, 1].

especially at the minimum depth (4 %); the cause primarily being due to the strong scattering of light by the stainless-steel knife edge used in their study. This resulted in the decrease in the PIV velocity data that is apparent near the knife edge.

Figure 9 demonstrates that the present non-Newtonian model predicts the flow reasonably well at all depths. The relatively high level of experimental uncertainty along with the fact that measurements are not available over a wide range of Reynolds numbers, do not warrant at this stage an attempt to systematically vary all the system parameters. The fit, which was made with only a handful of combinations of Bo and τ shows that the essential features of the flow are well captured at all three depths with $Bo = 3$ and $\tau = 1$. On the other hand, the response of DPPC at this surface packing is not captured as well by the Newtonian interface model. The Newtonian model did capture the flow of the monolayers at lower surface packing with a single parameter, Bo. Figure 9(*a*) shows that in order for a Newtonian model to fit the measurements in the region inside the knife edge, a relatively large value of Bo must be used. As the Bo for the model is increased, the over prediction of the flow speed outside of the knife edge ($1 < r < 2$) becomes even worse. This exercise shows that as the packing of DPPC is increased and the monolayer transitions to a solid phase (McConnell 1991), the interface responds to shear in a non-Newtonian fashion and that this change can be observed through measurements of the bulk flow that is driven by the interface. The simulation results using the non-Newtonian interfacial model capture this effect in figure 9(*d–f*). In particular, the model captures the correct slope and curvature near $r = 2$ while retaining a good fit for small r. Figure 10 shows how the different modelling of the interface affects the bulk flow, which is what was measured in the experiments of Raghunandan *et al.* (2015).

Predictive modelling of Newtonian interfaces has already been demonstrated for numerous insoluble monolayers over a wide range of shearing flow conditions. Specifically, for an interfacial film at a given surface packing (e.g. a Langmuir monolayer at a given surface pressure), a single value of the surface shear viscosity is able to provide excellent predictions of the interfacial velocity profile across the width of a deep-channel surface viscometer over a range of a few orders of magnitude in Reynolds number. In some cases, interfaces depart from this 'fluid' response when they are at large concentrations, and the interface is said to transition to a 'solid' phase. These various phases of interfacial films are well established (McConnell 1991; Adamson & Gast 1997).

The non-Newtonian constitutive relation for the interface used here is characterized by three parameters, Bo, ξ and τ. The Boussinesq number Bo is the non-dimensional

surface shear viscosity in the limit of infinite shear rate. The parameter ξ quantifies the maximal degree of shear thinning that is possible; it is the ratio of the surface shear viscosity at infinite shear rate to that in the limit of zero shear rate. The parameter τ quantifies the interfacial shear rate above which the interfacial stress does not exhibit shear-thinning behaviour. In certain limits, $\tau \to 0$ or $\xi \to 1$, the non-Newtonian model reduces to the usual shear-rate-independent Newtonian model, where the response to shear is solely described by the shear-rate-independent Bo. Non-zero values of τ or values of ξ different from one may capture the shearing response of interfaces of interest. For such shear-thinning interfaces, ξ is a material property (i.e. dependent on surface packing but not shear rate) since it is the ratio of the surface shear viscosities. Also, Bo is a ratio of two viscosities, the surface shear viscosity in the limit of infinite shear rate to the bulk fluid viscosity (times a length scale to make Bo non-dimensional).

The present interfacial model provides a foundation for investigating various aspects of interfacial hydrodynamics. For example, it would be interesting to investigate whether $\tilde{\tau}$ (the dimensional form of τ) is a material property for DPPC, for example. This would be the case if the constitutive relation accurately describes the shear-rate dependence of μ^s_{eff}. Velocity measurements over a wide range of knife-edge radii a, and rotation rates Ω, would be needed to verify whether or not $\tilde{\tau}$ is indeed a material property for a monolayer at a given surface packing.

There is an abundance of data in the literature showing surface shear viscosity as a function of 'shear rate' for numerous interfaces. However, these data generally come from a single measurement of torque or force assuming the Boussinesq number to be large and an idealized interfacial velocity profile. Most studies of interfacial rheology do not include velocity field measurements at the interface, let alone in the bulk. By not taking two-way coupling into account, it is difficult to separate coupling effects from non-Newtonian interfacial effects. In the present model the bulk flow is always accounted for, and so observed qualitative changes in the system response as the driving parameters are varied can be distinguished between effects due to coupling and effects due to changes in the interfacial flow regime.

Acknowledgements

We thank A. Raghunandan for his comments on this manuscript. This work was supported by NASA grant NNX13AQ22G.

Appendix A. Analytic solution in the limit $Bo \to \infty$

In this appendix we show the exact solution to the interfacial velocity profile in the limit $Bo \to \infty$. Solving the quadratic equation (3.3) for the positive solution gives

$$|S| = \frac{1}{2}\left(-\tau + \frac{C}{r^2}\right) + \frac{1}{2r^2}\sqrt{(\tau r^2 - C)^2 + 4\xi C\tau r^2}. \tag{A 1}$$

To obtain the interfacial azimuthal velocity v, it is convenient to define a local angular velocity $\omega = v/r$, such that $S = r\,\mathrm{d}\omega/\mathrm{d}r$. Combining this with (A 1) and recalling that the shear rate is negative ($S = -|S|$), gives

$$\frac{\mathrm{d}\omega}{\mathrm{d}r} = \frac{1}{2}\left(\frac{\tau}{r} - \frac{C}{r^3}\right) - \frac{1}{2r^3}\sqrt{(\tau r^2 - C)^2 + 4\xi C\tau r^2}. \tag{A 2}$$

Integrating (A 2) gives

$$\begin{aligned}\omega \;=\; & B+\frac{1}{2}\tau\ln r+\frac{C}{4r^2}+\frac{1}{2}\tau(1-2\xi)\ln r+\frac{1}{4r^2}\sqrt{(\tau r^2-C)^2+4\xi C\tau r^2}\\ & -\frac{\tau}{4}\ln\left[\tau r^2-C(1-2\xi)+\sqrt{(\tau r^2-C)^2+4\xi C\tau r^2}\right]\\ & -\frac{\tau(1-2\xi)}{4}\ln\left[C-\tau r^2(1-2\xi)+\sqrt{(\tau r^2-C)^2+4\xi C\tau r^2}\right].\end{aligned}\tag{A 3}$$

The constants C and B are determined by the boundary conditions. In terms of ω these are $\omega|_{r=1}=1$ and $\omega|_{r=A_R}=0$. The condition at $r=1$ can be used to replace B to obtain

$$\begin{aligned}\omega = 1+\tau(1-\xi)\ln r+\frac{C}{4r^2}-\frac{C}{4}+\frac{1}{4r^2}\sqrt{(\tau r^2-C)^2+4\xi C\tau r^2}-\frac{1}{4}\sqrt{(\tau-C)^2+4\xi C\tau}\\ -\frac{\tau}{4}\ln\left[\frac{\tau r^2-C(1-2\xi)+\sqrt{(\tau r^2-C)^2+4\xi C\tau r^2}}{\tau-C(1-2\xi)+\sqrt{(\tau-C)^2+4\xi C\tau}}\right]\\ -\frac{\tau(1-2\xi)}{4}\ln\left[\frac{C-\tau r^2(1-2\xi)+\sqrt{(\tau r^2-C)^2+4\xi C\tau r^2}}{C-\tau(1-2\xi)+\sqrt{(\tau-C)^2+4\xi C\tau}}\right].\end{aligned}\tag{A 4}$$

The constant C is determined by the condition at $r=A_R$, which is

$$\begin{aligned}0 \;=\; & 1+\tau(1-\xi)\ln A_R+\frac{C}{4A_R^2}-\frac{C}{4}\\ & +\frac{1}{4A_R^2}\sqrt{(\tau A_R^2-C)^2+4\xi C\tau A_R^2}-\frac{1}{4}\sqrt{(\tau-C)^2+4\xi C\tau}\\ & -\frac{\tau}{4}\ln\left[\frac{\tau A_R^2-C(1-2\xi)+\sqrt{(\tau A_R^2-C)^2+4\xi C\tau A_R^2}}{\tau-C(1-2\xi)+\sqrt{(\tau-C)^2+4\xi C\tau}}\right]\\ & -\frac{\tau(1-2\xi)}{4}\ln\left[\frac{C-\tau A_R^2(1-2\xi)+\sqrt{(\tau A_R^2-C)^2+4\xi C\tau A_R^2}}{C-\tau(1-2\xi)+\sqrt{(\tau-C)^2+4\xi C\tau}}\right].\end{aligned}\tag{A 5}$$

For general values of A_R, τ and ξ, the value of C must be determined numerically. Once the numerical value of C is determined, it can be used in (A 4), and then $v=r\omega$ gives

$$\begin{aligned}v \;=\; & r+\tau(1-\xi)r\ln r+\frac{C}{4r}-\frac{Cr}{4}+\frac{1}{4r}\sqrt{(\tau r^2-C)^2+4\xi C\tau r^2}-\frac{r}{4}\sqrt{(\tau-C)^2+4\xi C\tau}\\ & -\frac{\tau r}{4}\ln\left[\frac{\tau r^2-C(1-2\xi)+\sqrt{(\tau r^2-C)^2+4\xi C\tau r^2}}{\tau-C(1-2\xi)+\sqrt{(\tau-C)^2+4\xi C\tau}}\right]\\ & -\frac{\tau r(1-2\xi)}{4}\ln\left[\frac{C-\tau r^2(1-2\xi)+\sqrt{(\tau r^2-C)^2+4\xi C\tau r^2}}{C-\tau(1-2\xi)+\sqrt{(\tau-C)^2+4\xi C\tau}}\right].\end{aligned}\tag{A 6}$$

REFERENCES

ADAMSON, A. W. & GAST, A. P. 1997 *Physical Chemistry of Surfaces*, 6th edn. Wiley-Interscience.

BIRD, B. R., ARMSTRONG, R. C. & HASSAGER, O. 1987 *Dynamics of Polymeric Liquids, Volume 1: Fluid Mechanics*. Wiley.

CHOI, S. Q., STELTENKAMP, S., ZASADZINSKI, J. A. & SQUIRES, T. M. 2011 Active microrheology and simultaneous visualization of sheared phospholipid monolayers. *Nat. Commun.* **2**, 312.

DHAR, P., CAO, Y., FISCHER, T. M. & ZASADZINSKI, J. A. 2010 Active interfacial shear microrheology of aging protein films. *Phys. Rev. Lett.* **104**, 016001.

EDWARDS, D. A., BRENNER, H. & WASAN, D. T. 1991 *Interfacial Transport Processes and Rheology*. Butterworth-Heinemann.

ELFRING, G., LEAL, L. G. & SQUIRES, T. M. 2016 Surface viscosity and Marangoni stresses at surfactant laden interfaces. *J. Fluid Mech.* **792**, 712–739.

ERNI, P. 2011 Deformation modes of complex fluid interfaces. *Soft Matt.* **7**, 7586–7600.

ESPINOSA, G., LÓPEZ-MONTERO, I., MONROY, F. & LANGEVIN, D. 2011 Shear rheology of lipid monolayers and insights on membrane fluidity. *Proc. Natl Acad. Sci. USA* **108**, 6008–6013.

FULLER, G. G. & VERMANT, J. 2011 Editorial: dynamics and rheology of complex fluid–fluid interfaces. *Soft Matt.* **7**, 7583–7585.

FULLER, G. G. & VERMANT, J. 2012 Complex fluid–fluid interfaces: rheology and structure. *Annu. Rev. Chem. Biomol. Engng* **3**, 519–543.

GAUCHET, S., DURAND, M. & LANGEVIN, D. 2015 Foam drainage. Possible influence of a non-Newtonian surface shear viscosity. *J. Colloid Interface Sci.* **449**, 373–376.

HIRSA, A. H., LOPEZ, J. M. & MIRAGHAIE, R. 2002 Determination of surface shear viscosity via deep-channel flow with inertia. *J. Fluid Mech.* **470**, 135–149.

IVANOVA, A. N., IGNES-MULLOL, J. & SCHWARTZ, D. K. 2001 Microrheology of a sheared Langmuir monolayer: elastic recovery and interdomain slippage. *Langmuir* **17**, 3406–3411.

JIANG, T.-S., CHEN, J.-D. & SLATTERY, J. C. 1983 Nonlinear interfacial stress-deformation behavior measured with several interfacial viscometers. *J. Colloid Interface Sci.* **96**, 7–19.

KIM, K. H., CHOI, S. Q., ZASADZINSKI, A. & SQUIRES, T. M. 2011 Interfacial microrheology of DPPC monolayers at the air–water interface. *Soft Matt.* **7**, 7782–7789.

KURNAZ, M. L. & SCHWARTZ, D. K. 1997 Channel flow in a Langmuir monolayer: unusual velocity profiles in a liquid-crystalline mesophase. *Phys. Rev.* E **56**, 3378–3384.

LANGEVIN, D. 2014*a* Rheology of adsorbed surfactant monolayers at fluid surfaces. *Annu. Rev. Fluid Mech.* **46**, 47–65.

LANGEVIN, D. 2014*b* Surface shear rheology of monolayers at the surface of water. *Adv. Colloid Interface Sci.* **207**, 121–130.

LOPEZ, J. M. & HIRSA, A. H. 2015 Coupling of the interfacial and bulk flow in knife-edge viscometers. *Phys. Fluids* **27**, 042102.

MAESTRO, A., BONALES, L. J., RITACCO, H., FISCHER, T. M., RUBIO, R. G. & ORTEGA, F. 2011 Surface rheology: macro- and microrheology of poly(tert-butyl acrylate) monolayers. *Soft Matt.* **7**, 7761–7771.

MANNHEIMER, R. J. & SCHECHTER, R. S. 1970 An improved apparatus and analysis for surface rheological measurements. *J. Colloid Interface Sci.* **32**, 195–211.

MCCONNELL, H. M. 1991 Structures and transitions in lipid monolayers at the air–water interface. *Annu. Rev. Phys. Chem.* **42**, 171–195.

ORTEGA, F., RITACCO, H. & RUBIO, R. G. 2010 Interfacial microrheology: particle tracking and related techniques. *Curr. Opin. Colloid Interface Sci.* **15**, 237–245.

RAGHUNANDAN, A., LOPEZ, J. M. & HIRSA, A. H. 2015 Bulk flow driven by a viscous monolayer. *J. Fluid Mech.* **785**, 283–300.

REYNAERT, S., BROOKS, C. F., MOLDENAERS, P., VERMANT, J. & FULLER, G. G. 2008 Analysis of the magnetic rod interfacial stress rheometer. *J. Rheol.* **52**, 261–285.

SADOUGHI, A. H., LOPEZ, J. M. & HIRSA, A. H. 2013 Transition from Newtonian to non-Newtonian surface shear viscosity of phospholipid monolayers. *Phys. Fluids* **25**, 032107.

SAGIS, L. M. C. 2010 Modelling surface rheology of complex interfaces with extended irreversible thermodynamics. *Physica* A **389**, 673–684.

SAGIS, L. M. C. 2011 Dynamic properties of interfaces in soft matter: experiments and theory. *Rev. Mod. Phys.* **83**, 1367–1403.

SHLOMOVITZ, R., EVANS, A. A., BOATWRIGHT, T., DENNIN, M. & LEVINE, A. J. 2013 Measurement of monolayer viscosity using noncontact microrheology. *Phys. Rev. Lett.* **110**, 137802.

SLATTERY, J. C., SAGIS, L. & OH, E.-S. 2007 *Interfacial Transport Phenomena*, 2nd edn. Springer.

VANDEBRIL, S., FRANCK, A., FULLER, G. G., MOLDNAERS, P. & VERMANT, J. 2010 A double wall-ring geometry for interfacial shear rheology. *Rheol. Acta* **49**, 131–144.